Applied Catalysis B: Environmental 180 (2016) 372–378

Contents lists available at ScienceDirect

Applied Catalysis B: Environmental

journal homepage: www.elsevier.com/locate/apcatb

Enhancement in carbon dioxide activity and stability on nanostructured silver electrode and the role of oxygen

Michael Shincheon Jee[a,b], Hyo Sang Jeon[a,c], Cheonghee Kim[a], Hangil Lee[d], Jai Hyun Koh[a], Jinhan Cho[b], Byoung Koun Min[a,c,e,*], Yun Jeong Hwang[a,c,*]

[a] Clean Energy Research Center, Korea Institute of Science and Technology, 39-1 Hawolgok-dong, Seongbuk-gu, Seoul 136-791, Republic of Korea
[b] Department of Chemical and Biological Engineering, Korea University, Anam-dong, Seongbuk-gu, Seoul 136-713, Republic of Korea
[c] Korea University of Science and Technology, 217 Gajungro, Yuseong-gu, Daejeon 305-350, Republic of Korea
[d] Department of Chemistry, Sookmyung Women's University, Seoul 140-742, Republic of Korea
[e] Green School, Korea University, Anam-dong, Seongbuk-gu, Seoul 136-713, Republic of Korea

ARTICLE INFO

Article history:
Received 23 January 2015
Received in revised form 18 May 2015
Accepted 22 June 2015
Available online 29 June 2015

Keywords:
Electrochemical CO_2 reduction
Nanoparticle
Silver
Overpotential
Cyclic voltammetry

ABSTRACT

Current energy production habits deplete fossil fuels and accumulate atmospheric CO_2, which contribute to the global climate change. Electrochemical fuel production *via* CO_2 reduction reaction is an idealistic yet an achievable process that mitigates CO_2 emissions and simultaneously satisfies energy demands. Here, the enhancement of CO_2 reduction activity and stability on size-controlled particulate Ag electrocatalysts derived from a simple, one-step cyclic voltammetry (CV) process by changing scan rates (1–200 mV/s) was demonstrated. Interestingly, larger nanoparticles prepared by slower scan rates (1–5 mV/s) have exhibited the most degree of enhancement for CO_2 reduction to CO product. Compared to untreated Ag foil, nanostructured Ag electrode has shown an anodic shift of approximately 200 mV in the onset potential of CO partial current density (j_{CO}), 160 mV reduction of overpotential at j_{CO} = 10 mA/cm^2, and increased Faradaic efficiency (F.E.) for CO production especially at lower biased potentials (−0.89 to −1.19 V *vs.* RHE). Stability tests have demonstrated a drastic improvement in maintaining CO F.E. X-ray photoelectron spectroscopy suggests that the enhancement is associated with stable oxygen species incorporated on the nanoparticle Ag surfaces during the CV fabrication process.

© 2015 Elsevier B.V. All rights reserved.

1. Introduction

The global dependence on fossil fuel is not only depleting their stock but is contributing the climate change due to CO_2 emission during energy production [1,2]. Electrochemical CO_2 reduction reaction (CO_2RR) is an attractive process that reconverts the greenhouse gas into valuable carbon compounds which decreases their atmospheric concentration and stores energy into chemical bonds at the same time [3]. Essentially being the reverse reaction of combustion, CO_2RR is unfortunately endothermic and requires an external energy source that ultimately should not be from fossil fuels. Coincidentally, since many emerging renewable energies (such as solar and wind energies) have an issues with storing electricity, integration with CO_2RR may mutually eliminate each other's disadvantages.

Although idealistically convenient, this is a challenging task technically because of the thermodynamically stable conformation of CO_2. Hori et al. extensively studied the electrochemical CO_2 reduction activity on various metal foils but none were found to satisfy the material cost, product selectivity, long term stability, efficiency and safety requirements to be competitive in the economic market [4]. Another difficulty of electrochemical CO_2RR is the prevalence competing hydrogen evolution reaction (HER) and low CO_2 solubility in aqueous solution, while nonaqeuous or aprotic solution applications are often environmentally unfriendly and seldom produce high current density due to high solution resistance.

Moreover, density function theory (DFT) calculations estimated that it is difficult for individual bulk metals to selectively reduce CO_2 to CO at low overpotentials since their COOH binding energy and CO binding energy coordinates follow a trend line that lies in tangent to the kinetic volcano for CO evolution [5]. DFT calculations for CO_2 conversion to CH_4 and CH_3OH also follow similar

* Corresponding authors at: Clean Energy Research Center, Korea Institute of Science and Technology, 39-1 Hawolgok-dong, Seongbuk-gu, Seoul 136-791, Republic of Korea. Fax: +82 2 958 5809.
E-mail addresses: bkmin@kist.re.kr (B.K. Min), yjhwang@kist.re.kr (Y.J. Hwang).

http://dx.doi.org/10.1016/j.apcatb.2015.06.046
0926-3373/© 2015 Elsevier B.V. All rights reserved.

volcano plot correlation [6]. To overcome these limitations, another set of DFT calculations also hint that covalent embedment of Ag surfaces with p-block elements like S and Se could enhance the electrochemical CO_2 reduction activity by modulating COOH and CO binding free energies [7]. Additionally, research strategies that apply nanoparticles or nanostructured surfaces have demonstrated enhanced catalytic CO_2RR activities in terms of overpotential and product selectivity; however, exact reason for enhancement effects still remains controversial and requires more studies [8–16].

Among various techniques to fabricate nanostructured metal surfaces, reduction of metal oxides showed promising results in electrochemical CO_2RR application. Representative of these results are modified Au and Cu surfaces through pulsed anodization of the former or thermal oxidation of the latter and subsequent reduction of their oxides, which were found to greatly enhance the intrinsic catalytic activity toward CO_2 reduction by Kanan Group [8,9]. Even most recently, oxide-derived Pb was reported to form HCO_2^- selectively by suppressing HER [10]. Unfortunately, Au is one of the most expensive noble metal, Cu has poor selectivity among its several hydrocarbon products, and Pb is notoriously toxic. On the other hand, Ag is nontoxic, significantly cheaper than Au, and also has a high selectivity toward CO, a precursor in the Fischer–Tropsh process, despite relatively large overpotential required for CO production compared to Au. For reference, previous works concerning CO_2 reduction on Ag include bare surfaces [17], nanoparticles [11,12], and nanoporous [13] structures which suggest morphology of Ag is important in determining CO_2 reduction activity. As of yet, nanostructured Ag induced from silver oxide have not been studied for CO_2RR electrocatalysts.

Here, we demonstrate that nanostructure formation of Ag is possible when Ag is processed under cyclic voltammetry (CV) in a basic solution and can enhance CO_2RR activity and stability. This facile, one-step process has an added benefit of size-control by simply adjusting the scan rate [18]. This study has reveals an interesting perspective in the CO_2 reduction capability of nanostructured Ag electrodes fabricated at various scan rates. Contrary to our initial expectations, larger nanoparticles around 100–200 nm were found to have mostly enhanced CO_2RR activity toward CO evolution by reducing the required overpotential. In addition, nanostructured Ag samples also showed a remarkable stability in CO Faradaic efficiency (F.E.). Herein, properties and plausible reasons for the unusual CO_2 reduction activity of nanostructured Ag are presented.

2. Experimental

2.1. Preparation of nanostructured Ag

The p-Ag electrocatalyst sample was prepared by first mechanically polishing a Ag foil (25 × 25 × 0.5 mm, Dasom RMS) surface with 1.0 μm and 0.05 μm alumina polishing slurries (Micropolish®, Buhler) for 15 min each. After each polishing session, the Ag foil was generously washed with and ultrasonicated several times in deionized (DI) water to remove alumina residue and the unpolished reverse side was covered with electrically insulating tape. Then CV was performed in a beaker with 100 mL aqueous 0.1 M NaOH (98.0%, Samchun Chemicals) solution (pH 12.7) with the obverse side facing toward the Pt wire counter electrode and Ag/AgCl reference electrode. Each sample was subjected to five cycles of CV from −0.9 V to 1.0 V *vs.* Ag/AgCl at varying scan rates (1, 5, 50, and 200 mV/s) and was rinsed with DI water.

2.2. Electrochemical surface area measurement

Electrochemical surface area (ECSA) was measured by adopting an underpotential deposition (UPD) of Pb method [11,12]. CV was performed in aqueous 5 mM $Pb(NO_3)_2$ (≥99.0%, Sigma–Aldrich), 10 mM HNO_3, and 10 mM KCl (99.9%, Sigma–Aldrich) solution between −0.05 V and −0.50 V *vs.* Ag/AgCl at a scan rate of 10 mV/s.

2.3. CO_2 reduction reaction experiment

Electrochemical CO_2RR experiments were conducted in an airtight two-compartment polyether ether ketone (PEEK) cell separated by a proton exchange membrane (Nafion®, 117). Both compartments held 38 mL aqueous 0.5 M $KHCO_3$ (≥99.99%, Sigma–Aldrich) solution and were purged with 120 sccm CO_2 until saturated (pH 7.0) for 1 h before the experiment and the CO_2 flow was maintained for its duration. Working electrode (*i.e.*, mechanically polished Ag foil or p-Ag samples) and Ag/AgCl reference electrode were positioned in the catholyte that was stirred at 350 rpm with a magnetic stir bar and the Pt counter electrode was placed in the anolyte. A constant potential was applied with a potentiostat (Ivium, Iviumtechnology) and gaseous products were analyzed by gas chromatography (GC, Yonglin 6500) equipped with a capillary column (Restek, RT®-Msieve 5A) and pulsed discharge ionization detector (PDD) using ultra high purity (UHP, 99.9999%) He as the carrier gas. The F.E. of H_2 or CO was calculated according to the following equations,

$$i_{H_2/CO} = V_{H_2/CO} \times Q \times \frac{2Fp}{RT}$$

$$F.E._{H_2/CO} = \frac{i_{H_2/CO}}{i} \times 100$$

where $i_{H_2/CO}$ is the partial current density of H_2 or CO, $V_{H_2/CO}$ is the volume concentration of H_2 or CO measured by GC, Q is the flow rate measured by a universal flow meter (ADM 2000, Agilent Technologies) at the exit of the electrochemical cell, i is the total current density, F is the Faradaic constant, p is the pressure, T is the temperature, and R is the ideal gas constant.

Liquid products were also analyzed by ion chromatography (IC, DIONEX IC25A). The procedure was repeated for various potentials. Solution resistance, R_s, was measured by circle fitting the measurement taken from electrochemical impedance spectroscopy (EIS) and potential values were compensated for *iR* loss and converted in terms of reversible hydrogen electrode (RHE) by using the following equation:

$$E(vs.\text{RHE}) = E\left(vs.\text{Ag/AgCl}\right) + 0.197\text{V} + (0.0591 \times \text{pH})$$

2.4. Characterization

The surface morphologies were obtained by field emission gun scanning electron microscopy (FEG-SEM, Inspect F, FEI). The crystal structure was confirmed by measuring X-ray diffraction (XRD-6000, Shimadzu). To analyze the surface element composition, high-resolution X-ray photoelectron spectroscopy (XPS) experiments were performed at the 8A2 beamline at the Pohang Accelerator Laboratory (PAL), which was equipped with an electron analyzer (SES100, Gamma-Data Scienta). The Ag3d and O 1s core level spectra were obtained by using photon energies of 420 and 580 eV respectively to enhance the surface sensitivity. The binding energies of the core level spectra were determined with respect to the binding energies (E_B = 84.0 eV) of the clean Au 4*f* core level for the same photon energy. $^{13}CO_2$ isotope gas was purchased from Cambridge Isotope Laboratories and was conducted with a gas chromatograph (GC, 6890N network, Agilent Technologies) equipped with a mass-selective detector (MSD, 5973 network, Agilent Technologies).

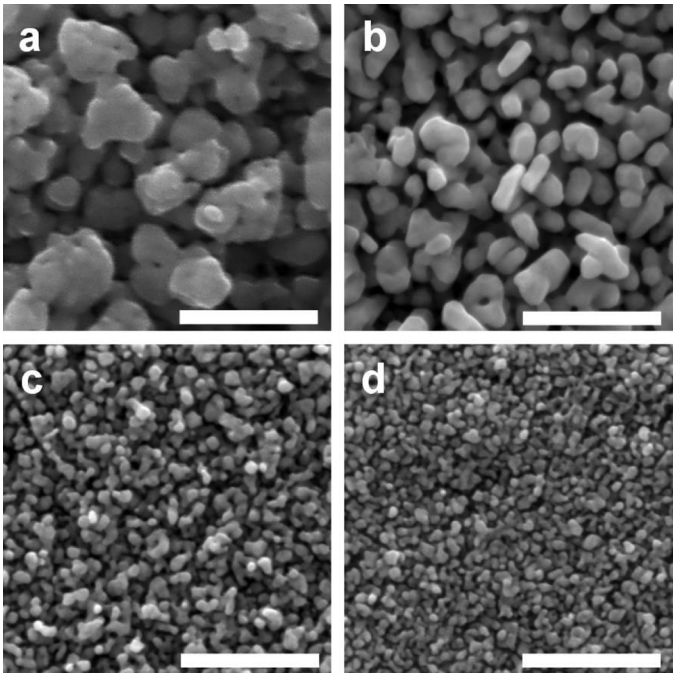

Fig. 1. (a–d) Scanning electron micrographs of p-Ag samples fabricated in 0.1 M NaOH after five cycles of cyclovoltammetry between −0.9 V and 1.0 V *vs.* Ag/AgCl at 1, 5, 50, and 200 mV/s, respectively (scale bar = 500 nm).

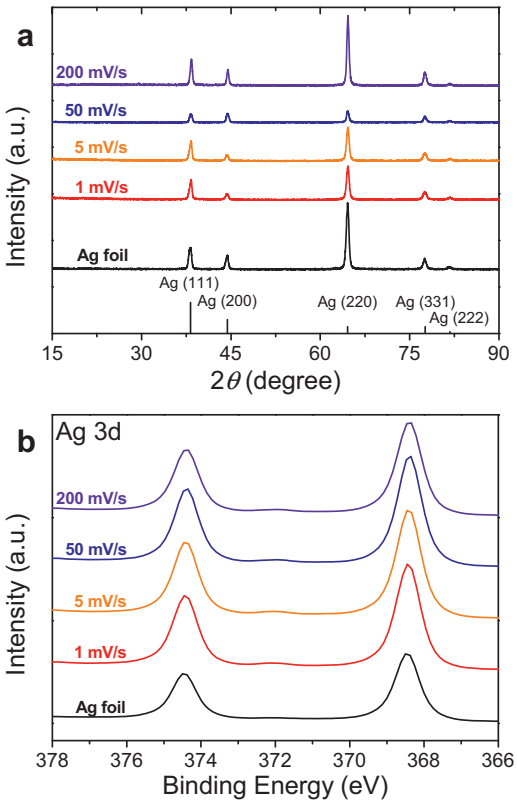

Fig. 2. (a) XRD patterns and (b) XPS Ag 3d peaks of untreated Ag foil and p-Ag samples fabricated at various scan rates.

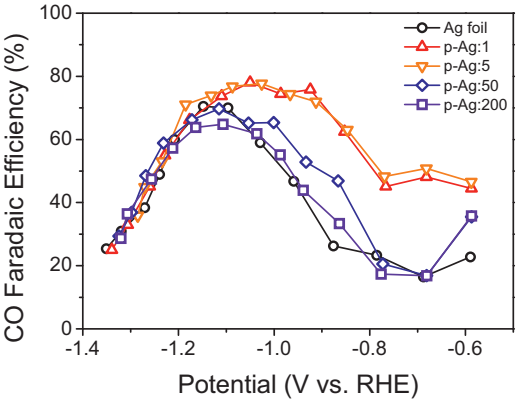

Fig. 3. CO F.E. *vs.* applied potential of Ag foil and p-Ag samples.

3. Results and discussion

CV of Ag foil in 0.1 M NaOH solution exhibited two distinct anodic peaks and two distinct cathodic peaks (Fig. S1), which respectively correspond to the formations and reductions of two silver oxides (Ag_2O and AgO). A less obvious oxidation peak at 0.20 V *vs.* Ag/AgCl is attributed to the formation of Ag_2O or AgOH monolayer. Peaks broaden and increase in current as scan rate increase, and the current saturates at the fifth cycle (Fig. S1(a)–(d)). Scanning electron microscopy (SEM) images show layer formations of 142 ± 44, 104 ± 33, 41 ± 11, and 28 ± 7.6 nm particles for Ag samples treated with scan rates at 1, 5, 50, and 200 mV/s (henceforth called p-Ag:1, p-Ag:5, p-Ag:50, and p-Ag:200; Fig. 1(a)–(d) and Table S1), respectively, compared to the featureless topology of the untreated Ag foil surface (Fig. S2(a)). Larger and less uniform nanostructures were obtained as the scan rate decreased, and curved structures were formed regardless of CV conditions. These nanostructured morphologies are consistent with observations by Wan et al. who reasoned that the smaller, more uniform size distribution is a consequence of less agglomeration time at higher scan rates. Conversely, at lower scan rates, nanocrystals have a longer period to agglomerate resulting in the larger and less uniform features [18].

Next, to estimate the surface area of the nanostructured p-Ag samples, electrochemical surface area (ECSA) measurements were taken, in which the roughness factors were derived from the integrals of the CV peaks corresponding to the underpotential deposition (UPD) of Pb (Fig. S3). Relative to that of Ag foil, the roughness factors were 7.65, 4.15, 2.38, and 1.72 for p-Ag:1, p-Ag:5, p-Ag:50, and p-Ag:200, respectively (Table S1). Despite smaller particles having greater surface-to-volume ratios, the unexpected increase in the ECSA with increasing particle size is attributed to the relatively thicker formation nanoparticle layers. This is evident as more charge passed during the formation and reduction in CV measurements at lower scan rates (Fig. S1(e)). Darker p-Ag samples were obtained as the scan rate decreased which also indicates thicker film formation of p-Ag.

X-ray diffraction (XRD) patterns for all samples show 2θ peaks at 38.2°, 44.4°, 64.6°, 77.6°, and 81.8° which all correspond to diffractions along the (1 1 1), (2 0 0), (2 2 0), (3 1 1), and (2 2 2) planes of the face-centered cubic Ag crystal structure (Fig. 2(a)). A particularly intense (2 2 0) peak for the Ag foil suggests a preferred crystal orientation. Meanwhile, the relative intensities of the each diffraction pattern for the p-Ag samples more closely resemble the powder Ag reference peaks from a crystallography database showing relative increase of (1 1 1) peak compared to the Ag foil. The exception of p-Ag:200 having a similar diffraction pattern to that of Ag foil is explained by the penetration depth of incident X-ray detecting the unaltered phase underneath the thinner nanoparticle layers. All of the XRD patterns were associated with the Ag crystal structure and no crystalline silver oxide phases were observed.

In addition, X-ray photoelectron spectroscopy (XPS) spectra show that Ag foil and all p-Ag samples have Ag 3d peaks at 368.4 eV

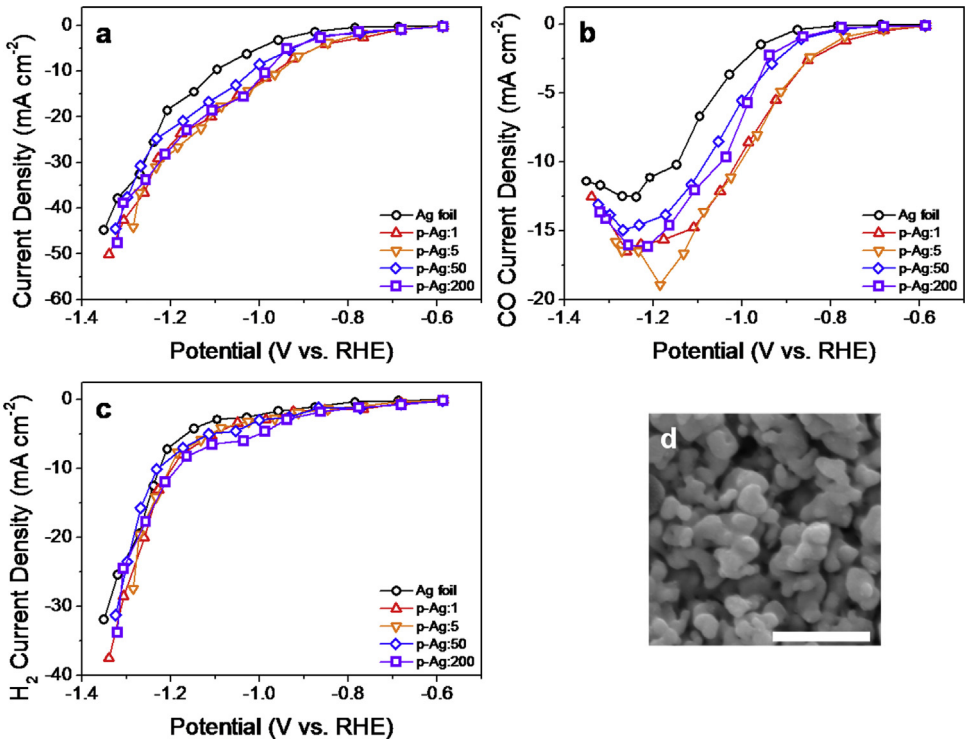

Fig. 4. (a) Total, (b) H_2 partial, and (c) CO partial current densities *vs.* applied potential of Ag foil and p-Ag samples. (d) SEM images of p-Ag:5 taken post-CO_2RR.

and 374.4 eV, which are assigned to Ag $3d_{5/2}$ and Ag $3d_{3/2}$ peaks, respectively (Fig. 2(b)). All p-Ag samples have similar binding energies of Ag 3d peaks with that of Ag foil, which suggests that Ag_2O or AgO formed during its fabrication was mostly reduced to metallic Ag upon completion of CV. Detailed XPS analysis revealed that there were two small Ag 3d peaks associated with oxidized Ag states for Ag foil as well as p-Ag samples, which are considered to be natively formed on the Ag surface (discussed below.) Even if there was small amount of residual silver oxide on the nanostructured p-Ag samples, they were expected to be reduced to Ag under the cathodic potentials applied during CO_2RR.

CO_2RR experiments for Ag foil and all p-Ag samples yielded CO as the main product with trace CH_4 (<1% F.E.) and balance H_2 (Fig. 3). Analysis of liquid products (such as formic acid) did not detect any concentrations above the IC's detection limit, which was consistent with the previous studies with polycrystalline Ag foil [4,17]. In other words, H_2 F.E. would be the complement of CO F.E. (or H_2 F.E. = 100% − CO F.E.) since H_2 and CO are the only species produced from the catholyte. The CO_2 reduction activity is enhanced in terms of required overpotential to achieve maximum F.E. for CO production as the scan rates applied to fabricate p-Ag decrease. Both of p-Ag:1 and p-Ag:5 electrodes had over 70% of CO F.E. at a potential as low as −0.89 V *vs.* RHE, which was 200 mV lower in overpotential compared to Ag foil (−1.09 V *vs.* RHE). In addition, comparing CO F.E. at the given bias potential (−0.89 V *vs.* RHE), the p-Ag:1 and p-Ag:5 electrodes achieved approximately 30% higher CO F.E. than Ag foil. Although having similar CO_2 reduction activities, p-Ag:5 was selected over p-Ag:1 as the optimal condition for comparison studies from here on due to the shorter preparation time.

The breadths of CO F.E. *vs.* applied potential curves (Fig. 3) tend to broaden toward lower overpotentials while converging at −1.20 V *vs.* RHE; for instance, only a single point reaches 70% CO F.E. at −1.12 V *vs.* RHE for Ag foil but for p-Ag:5 a "potential window" of 310 mV that satisfies similar CO F.E. range from −0.89 V to −1.18 V *vs.* RHE. The wide potential window is advantageous in applications, such as solar-fuel devices incorporated with a photovoltaic cell, because CO selectivity can be maintained even at variable operation potentials with small coupling loss [19]. Overall, Fig. 3 represents the evolution of CO_2RR activities, where the CO F.E. *vs.* applied potential curves for p-Ag:200 and p-Ag:50 gradually shifts from that of Ag foil to that of the most active p-Ag:5 and p-Ag:1.

Despite having different ECSA's, p-Ag samples merged to similar current densities at potentials greater than −1.10 V *vs.* RHE (Fig. 4(a)) most likely due to CO_2 mass transfer limitations. More interestingly, the onset potential of the CO partial current density shifts anodically with p-Ag samples compared to bulk Ag foil, and both p-Ag:1 and p-Ag:5 showed similar shifts by approximately 200 mV (Fig. 4(b)), which was consistent with the enhancement of CO F.E. results as shown in Fig. 3. Also, at CO partial current density of 10 mA/cm^2, a 160 mV reduction in the overpotential was measured with these two p-Ag samples. The onset potential shift and overpotential reduction also occurred for p-Ag:50 and p-Ag:200 albeit at a lesser extent (Table S1). Nevertheless, all p-Ag cathodes have has proven to catalytically reduce the overpotentials for CO_2 to CO production compared to polycrystalline Ag foil.

Previously, different Ag facets were reported to have some variance in the CO_2 reduction activity but Ag(1 1 1) and Ag(1 0 0) were catalytically inert relative to Ag(1 1 0) [20]. Because our p-Ag samples exhibited lower onset potentials than the most active Ag(1 1 0) facet, the enhanced activity cannot be explained with the mentioned Ag facets alone. Other reference on nanoporous Ag material speculates that high-index facets are more active toward CO_2 reduction in exhibiting a significant reduction in the overpotential. Meanwhile, the CO_2 electroreduction size-controlled nanoparticle study reports an improvement in the CO partial current density with no effect on the onset potential even though smaller nanoparticle have more high-index facets. Therefore, further studies are still required to understand the origins of decrease in overpotential with nanostructured CO_2 electrocatalysts.

From another perspective, the H_2 partial current densities of the electrochemically prepared p-Ag were compared in Fig. 4(c). At

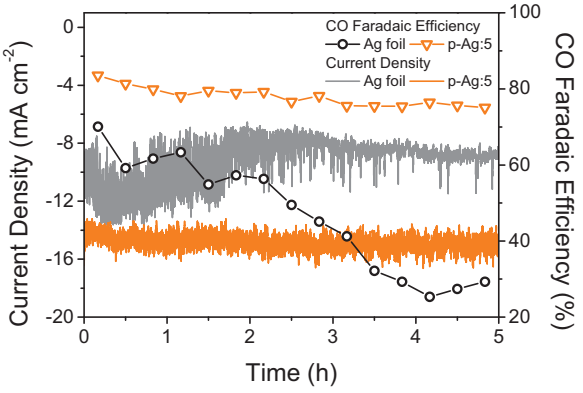

Fig. 5. (a) Total current densities and (b) CO F.E.'s of Ag foil and p-Ag:5 at −1.80 V *vs.* Ag/AgCl. The *iR*-corrected potentials are about −1.10 V and −1.04 V *vs.* RHE, respectively.

lower bias potential ranges from −0.95 V *vs.* RHE, p-Ag:50 and p-Ag:200 exhibited greater hydrogen evolution activity, while p-Ag:1 and p-Ag:5 approached comparable H_2 partial current densities with that of Ag foil. The divergence of H_2 partial current densities converges at higher bias potentials. The nonproportionality of H_2 evolution activity to the roughness factor indicates that HER active sites did not increase with increasing ECSA. Rather, smaller nanoparticles fabricated with higher scan rates are slightly more active toward HER at lower overpotentials, which may be related to the poorer CO_2RR activity with p-Ag:50 and p-Ag:200 than p-Ag:5. In other words, the electrochemical treatment of Ag surfaces was able to keep HER active sites relatively constant while increasing CO_2RR active sites, which, consequently, widened potential window for CO evolution.

In addition, SEM images of p-Ag:1 and p-Ag:5 (Figs. 4(d) and S2(b)) after CO_2RR lasting 2.5 h remained identical to the images before, while p-Ag:50 nanoparticles appeared to have agglomerated and p-Ag:200 became unrecognizable as the original nanoparticles disappeared (Fig. S2(c) and (d)) even after the same CO_2RR conditioning. We expect that the lower CO_2 reduction to CO production activity with p-Ag:200 as shown in Figs. 3 and 4 are associated with the changes of the nanostructures on the Ag electrode surface as well. It is interesting to note that these trends are contrary to the initial expectation that smaller nanoparticles have more edge or high index sites that are more active toward CO_2 reduction and better stabilize the CO_2^- intermediate [11–13]. p-Ag samples fabricated by our electrochemical methods showed that the optimal size of the nanoparticles were around 100–200 nm for CO_2RR, and the smaller sized particles (30–50 nm) had poor activities due to the tendency for agglomeration. Curiously, even comparing similar particle sizes, *i.e.*, pre-CO_2RR p-Ag:5 (Fig. 1(b)) and post-CO_2RR p-Ag:50 (Fig. S2(c)), yields differing CO F.E. profiles, which indicates that morphology is not the only factor that affects the activity and stability for CO_2RR with p-Ag samples and is discussed below.

To examine the CO_2RR activity further, the electrocatalytic stability of p-Ag:5 and Ag foil samples were compared by performing a durability test for 5 h under the same bias potential (Fig. 5). In both tests, −1.8 V *vs.* Ag/AgCl were applied to compare the samples at their maximum CO F.E. Throughout the 5 h stability test, both Ag foil and p-Ag:5 electrodes showed stable current densities, but the CO F.E. differences were dramatic. Although Ag foil was able to sustain an almost consistent current density, the CO F.E. continued to drop from 70.0% to 29.3% after 5 h. This implies that the initial active sites for CO_2RR for CO production convert to be more active toward HER. In comparison, p-Ag:5 maintained a constant current density throughout the electrocatalytic process and only dropped 8.4% from the initial 83.5% CO F.E. The unchanged morphology of p-Ag:5 after CO_2RR may have contributed to its enhanced stability.

Some insights may be drawn from electrochemical kinetics with Tafel analysis (Fig. S4). The Tafel slopes for both Ag foil and p-Ag samples were about 140 mV/dec indicating CO_2RR mechanism where single-electron transfer is the rate-limiting step for all samples. However, when comparing Ag foil to p-Ag:1 there was almost a two-magnitude increase in exchange current density which demonstrates an enhanced intrinsic catalytic activity through the increasing of kinetic constant for CO_2 reduction (Table S1). In addition, electrolysis with $^{13}CO_2$ isotope confirmed that the source of C was indeed from CO_2 and not the dissolved $KHCO_3$ in the electrolyte (Fig. S5). If the carbonate ions composed of nonspecific C isotopes were reduced, GC–MS would have detected ^{12}CO instead of ^{13}CO, but only ^{13}CO was detected proving CO_2 gas was the only C source in our reduction reaction.

Upon closer analysis with high resolution beamline XPS for three representative Ag samples (*i.e.* Ag foil, p-Ag:5, and p-Ag:50 samples) before and after CO_2RR, subtle yet significant differences in the surface electronic states of Ag and O species were discovered (Fig. 6). The *ex-situ* XPS elemental analysis measured surface oxygen contents of about 20 atomic% for all samples (Table S1) which can be formed under ambient condition. This observation lead to a hypothesis that natively adsorbed or residual surface oxygen species may have contributed to the CO_2RR activity. Oxygen has been shown to play a critical role in CO_2RR on the Sn/SnO_x thin-film electrocatalyst [21] and oxygen vacancy sites are thought to be the CO_2 reduction sites for TiO_2 and other metal oxide semiconductor photocatalysts [22]. Another study proposed that an ultrathin, kinetically stable oxide or hydroxide can suppresses HER [10].

All XPS measurements retained their major peaks at 368.4 eV and 374.4 eV for the two Ag 3d peaks (*i.e.,* Ag^0) and at 533.3 eV for O 1s (*i.e.,* adsorbed OH^- and H_2O). For simplicity, the Ag $3d_{5/2}$ peak will be described in detail over the Ag $3d_{3/2}$ peak, which is exactly identical. For all three samples, as-prepared pre-CO_2RR samples revealed same Ag $3d_{5/2}$ and O 1s spectra (Fig. 6(a) and (c)). There were similar two minor Ag $3d_{5/2}$ peaks at 368.9 and 367.9 eV (Fig. 6(a)), which are respectively associated with Ag^+ and Ag^{3+} states [23], and the O 1s spectra also contained a similar minor peak at 534.5 eV (Fig. 6(c)), which is attributed to oxygen in a strongly electronegative environment [24]. Note the proportions of the deconvoluted minor peaks were similar for these measurements indicating Ag foil and p-Ag samples have similar electronic states before CO_2RR. In addition, no O 1s peaks associated with metal oxides (*i.e.,* Ag_2O or AgO) were present (approximately 529 eV) for as prepared samples.

After CO_2RR, however, the minor peaks underwent a few changes, especially with O 1s spectra, depending on the Ag samples. The 368.9 and 367.9 eV of Ag $3d_{5/2}$ peaks were deintensified as the Ag^+ and Ag^{3+} states became reduced in the reductive condition of CO_2RR (Fig. 6(b)). More conspicuously, the 534.5 eV O 1s peak disappeared for both of Ag foil and p-Ag:50 samples (Fig. 6(d)); however, instead a new peak with lower binding energy appeared at 532.3 eV, which is attributed to surface-bound hydroxyl species [25]. On the other hand, 534.5 eV peak of the p-Ag:5 sample endured without an appearance of extra O 1s peaks even after CO_2RR, which implies that the CV process employed in this study may have formed a stable oxygen species on p-Ag:5 surface that is resistant to collateral damage even in the reductive environment of CO_2RR. The XPS results can explain the disparity in Ag foil and p-Ag:5 for CO_2RR activity and stability. Slower CV cycles of oxidation and subsequent reduction can affect oxygen species on p-Ag surfaces until a saturation in activity is achieved as seen in p-Ag:1 and p-Ag:5. Although, further studies are required to identify the nature of the oxygen species on the Ag surface, this hypothesis can be extended to other oxide-derived electrocatalysts which may also

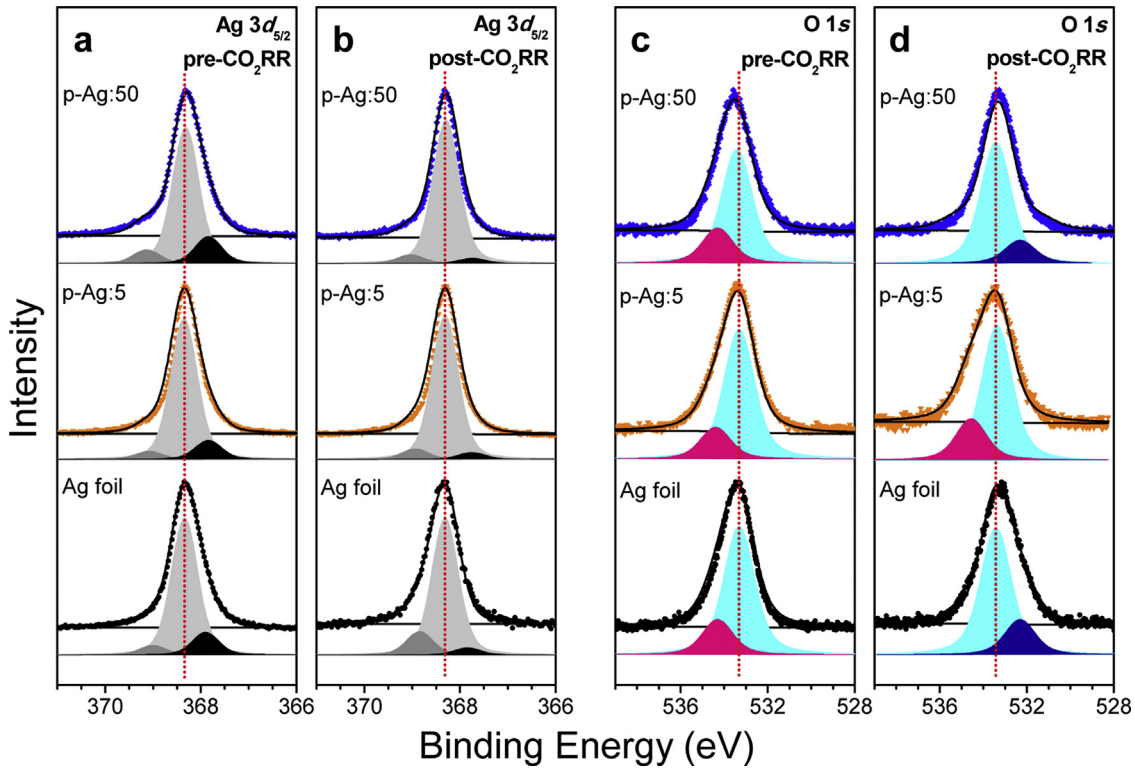

Fig. 6. Normalized XPS (a and b) Ag $3d_{5/2}$ and (c and d) O 1s peaks of untreated Ag foil, p-Ag:5, and p-Ag:50 (a and c) pre- and (b and d) post-CO_2RR. The deconvoluted peaks are offset from the fitted and base lines (black solid) for clarity. Vertical red dots are to guide the reader's eye to distinguish various species.

have residual oxygen content that contributes to the enhancement of CO_2RR.

The scope of this was study purposefully limited by having the CV scan rate be the only variable for designing a more complete set of experiments to better understand the origin for the enhanced electrochemical CO_2RR. It can be expected that other parameter modifications, such as adjusting the strength of the basic solution, using pulsed oxidation/reduction instead of CV, and even using different synthetic approaches of oxidation/reduction beyond an electrochemical method, could further optimize the catalytic properties. We hope that sharing such findings may contribute the academic community by furthering the scientific understanding of how CO_2 can be electrocatalytically reduced.

4. Conclusions

Improvement in CO_2 reduction activity and stability toward CO was achieved on p-Ag electrodes fabricated by a facile, one-step electrochemical CV process, in which Ag was repeatedly oxidized and reduced in a basic electrolyte. The sizes of the nanoparticles formed on the Ag foil were controlled in the range of 30–200 nm by varying the scan rate, whose influence on the CO_2RR activity yielded higher activity with larger sized p-Ag electrodes. More specifically, p-Ag:5 with approximately 100 nm nanoparticles was able to the shift onset potential of the CO partial current density anodically by approximately 200 mV and reduce the overpotential by 160 mV when compared to the untreated Ag foil. The 310 mV expansion of the CO F.E. potential window was possible due to the electrochemical treatment of Ag surfaces keeping HER active sites relatively constant while increasing the reaction sites active toward CO_2RR. Stability tests demonstrated a drastic improvement of CO F.E. stability where p-Ag:5 was able to maintain a stable current and CO F.E. The slower scan rate applied for p-Ag fabrication exhibited more enhanced CO_2RR activity, associated with stable oxygen species incorporated on Ag surfaces during the fabrication process.

Acknowledgements

This work was supported by the program of the Korea Institute of Science and Technology (KIST), and partly by the Korea Center for Artificial Photosynthesis (KCAP, 2014M1A2A2070004) and University-Institute Cooperation Program funded by the Minister of Science, ICT and Future Planning (MSIP) through the National Research Foundation of Korea.

Appendix A. Supplementary data

Supplementary data associated with this article can be found, in the online version, at http://dx.doi.org/10.1016/j.apcatb.2015.06.046

References

[1] G. Centi, E.A. Quadrelli, S. Perathoner, Energy Environ. Sci. 6 (2013) 1711–1731.
[2] J.A. Turner, Science 285 (1999) 1493.
[3] N.S. Lewis, D.G. Nocera, P. Natl. Acad. Sci. USA 103 (2006) 15729–15735.
[4] Y. Hori, Modern Aspects of Electrochemistry, in: C. Vayenas, R. White, M. Gamboa-Aldeco (Eds.), Springer, New York, 2008, pp. 89–189.
[5] H.A. Hansen, J.B. Varley, A.A. Peterson, J.K. Norskov, J. Phys. Chem. Lett. 4 (2013) 388–392.
[6] K.P. Kuhl, T. Hatsukade, E.R. Cave, D.N. Abram, J. Kibsgaard, T.F. Jaramillo, J. Am. Chem. Soc. 136 (2014) 14107–14113.
[7] H.K. Lim, H. Shin, W.A. Goddard, Y.J. Hwang, B.K. Min, H. Kim, J. Am. Chem. Soc. 136 (2014) 11355–11361.
[8] Y.H. Chen, C.W. Li, M.W. Kanan, J. Am. Chem. Soc. 134 (2012) 19969–19972.
[9] C.W. Li, M.W. Kanan, J. Am. Chem. Soc. 134 (2012) 7231–7234.
[10] C.H. Lee, M.W. Kanan, ACS Catal. 5 (2015) 465–469.
[11] A. Salehi-Khojin, H.R.M. Jhong, B.A. Rosen, W. Zhu, S.C. Ma, P.J.A. Kenis, R.I. Masel, J. Phys. Chem. C 117 (2013) 1627–1632.
[12] S. Ma, Y. Lan, G.M.J. Perez, S. Moniri, P.J.A. Kenis, ChemSusChem 7 (2014) 866–874.

[13] Q. Lu, J. Rosen, Y. Zhou, G.S. Hutchings, Y.C. Kimmel, J.G. Chen, F. Jiao, Nat. Commun. 5 (2014) 1–6.
[14] W. Zhu, R. Michalsky, Ö. Metin, H. Lv, S. Guo, C.J. Wright, X. Sun, A.A. Peterson, S. Sun, J. Am. Chem. Soc. 135 (2013) 16833–16836.
[15] W. Zhu, Y.-J. Zhang, H. Zhang, H. Lv, Q. Li, R. Michalsky, A.A. Peterson, S. Sun, J. Am. Chem. Soc. 136 (2014) 16132–16135.
[16] W. Tang, A.A. Peterson, A.S. Varela, Z.P. Jovanov, L. Bech, W.J. Durand, S. Dahl, J.K. Norskov, I. Chorkendorff, Phys. Chem. Chem. Phys. 14 (2012) 76–81.
[17] T. Hatsukade, K.P. Kuhl, E.R. Cave, D.N. Abram, T.F. Jaramillo, Phys. Chem. Chem. Phys. 16 (2014) 13814–13819.
[18] Y. Wan, X.L. Wang, S.Y. Liu, Y.B. Li, H. Sun, Q. Wang, Int. J. Electrochem. Sci. 8 (2013) 12837–12850.
[19] H.S. Jeon, J.H. Koh, S.J. Park, M.S. Jee, D.-H. Ko, Y.J. Hwang, B.K. Min, J. Mater. Chem. A 3 (2015) 5835–5842.
[20] N. Hoshi, M. Kato, Y. Hori, J. Electroanal. Chem. 440 (1997) 283–286.
[21] Y.H. Chen, M.W. Kanan, J. Am. Chem. Soc. 134 (2012) 1986–1989.
[22] S.N. Habisreutinger, L. Schmidt-Mende, J.K. Stolarczyk, Angew. Chem. Int. Ed. 52 (2013) 7372–7408.
[23] D. Lutzenkirchen-Hecht, H.H. Strehblow, Surf. Interface Anal. 41 (2009) 820–829.
[24] K.L. Mittal, Polymer Surface Modification: Relevance to Adhesion, Taylor & Francis, 2000.
[25] H.S. Casalongue, S. Kaya, V. Viswanathan, D.J. Miller, D. Friebel, H.A. Hansen, J.K. Norskov, A. Nilsson, H. Ogasawara, Nat. Commun. 4 (2013) 1–6.